Published in final edited form as:
Biochemistry. 2013 February 26; 52(8): . doi:10.1021/bi301613p.

Reversible phenol oxidation-reduction in the structurally well-defined 2-mercaptophenol-α_3C protein[†,‡]

Cecilia Tommos[*], **Kathleen G. Valentine**, **Melissa C. Martínez-Rivera**, **Li Liang**, and **Veronica R. Moorman**
Graduate Group in Biochemistry & Molecular Biophysics and Department of Biochemistry & Biophysics, University of Pennsylvania, Philadelphia, Pennsylvania 19104-6059

Abstract

2-mercaptophenol-α_3C serves as a biomimetic model for enzymes that use tyrosine residues in redox catalysis and multistep electron transfer. This model protein was tailored for electrochemical studies of phenol oxidation-reduction with specific emphasis on the redox-driven protonic reactions occurring at the phenol oxygen. This protein contains a covalently modified 2-mercaptophenol-cysteine residue. The radical site and the phenol compound were specifically chosen to bury the phenol OH group inside the protein. A solution nuclear magnetic resonance structural analysis: (i) demonstrates that the synthetic 2-mercaptophenol-α_3C model protein behaves structurally as a natural protein, (ii) confirms the design of the radical site, (iii) reveals that the ligated phenol forms an inter helical hydrogen bond to glutamate-13 (phenol oxygen/carboxyl oxygen distance 3.2 ± 0.5 Å), and (iv) suggests a proton-transfer pathway from the buried phenol OH (average solvent accessible surface area of 3 ± 5%) via glutamate-13 (average solvent accessible surface area of the carboxyl oxygens 37 ± 18%) to the bulk solvent. A square-wave voltammetry analysis of 2-mercaptophenol-α_3C further demonstrates: (v) that the phenol oxidation-reduction cycle is reversible, (vi) that formal reduction potentials can be obtained, and (vii) that the phenol-O$^\bullet$ state is long lived with an estimated lifetime of ≥ 180 milliseconds. These properties make 2-mercaptophenol-α_3C a unique system to characterize phenol-based proton-coupled electron transfer in a low dielectric and structured protein environment.

Tyrosine serves as a one-electron redox cofactor in proteins and may form three redox pairs: Y-OH$^{\bullet+}$/Y-OH, Y-O$^\bullet$/Y-OH and Y-O$^\bullet$/Y-O$^-$ (1-5). The pK_a of aqueous tyrosine in its oxidized and reduced state are −2 and 10, respectively. This predicts that Y-O$^\bullet$/Y-OH is the dominating redox couple in a protein environment (1). Thus, oxidation-reduction of protein tyrosine residues is coupled to de- and reprotonation at the phenol oxygen. Mechanistically, these electron and proton transfers may occur along concerted or stepwise pathways and significant efforts are being made to experimentally characterize these types of proton-coupled electron transfer (PCET) reactions and form a theoretical framework for PCET processes in proteins (4-10).

[†]Funding was provided by NIH grant GM079190 and by NIH predoctoral fellowship GM096756 to M.C.M.R.

[‡]RCSB PDB ID, 2LXY; BMRB accession number 18703

[*]CORRESPONDING AUTHOR FOOTNOTE: All correspondence should be addressed to: 905 Stellar-Chance Laboratories, Department of Biochemistry & Biophysics University of Pennsylvania, 422 Curie Blvd, Philadelphia, PA 19104-6059 Telephone: 215-746-2444; Facsimile:, 215-573-7290; tommos@mail.med.upenn.edu.

SUPPORTING INFORMATION AVAILABLE. 2MP-α_3C/PGE working electrode optimization and control experiments (Fig. S1–S4); diffusion attenuation plot (Fig. S5). Designations used for the unnatural 2MP-C32 residue (Table S1); $^3J_{HNHA}$ coupling constants and Random Coil Index values obtained for 2MP-α_3C (Table S2); SASA values for all 2MP-α_3C residues (Table S3); atom-level SASA values for 2MP-C32 and E13 (Table S4). This material is available free of charge via the internet at http://pubs.acs.org.

The model approach to study tyrosine-based PCET spans from free phenol in neat water to engineering of natural proteins (e.g. 11-25). The *de novo* α_3X radical proteins were developed as part of this effort (3, 26, 27). Scheme 1 shows the amino acid sequence of the three-helix bundle that forms the structural platform for the α_3X system.

GSR(1)•**V**KA**L**EEK•**V**KA**L**EEK•**V**K–*A**L**GGGG*–R•**I**EE**L**KKK•**X(32)**EE**L**KKK•**I**EE–*L**GGGGE*–

•**V**KK**V**EEE•**V**KK**L**EEE•**I**KK*L(65)*

(Scheme 1)

The sequence is based on the classic heptad-repeat design of α-helical coiled coils and bundles (28). The 7-residue heptads, with internal positions labeled *a* through *g*, are marked by bullets. The N-terminal GS residues (in grey) form part of a thrombin cleavage site and are labeled as −2 and −1 to keep the amino-acid numbering consistent between the chemically synthesized (65 residues; 26) and recombinantly expressed (66-67 residues; 29, 30) α_3X proteins. The radical site (position 32, in red) is located in the middle of the central helix and occupied by a tyrosine (to form the α_3Y protein), a cysteine (α_3C) or a tryptophan (α_3W).

α_3Y is an electrochemically reversible system with a long-lived tyrosine radical (31). The radical site in α_3Y was designed to completely shield Y32 from the bulk solvent (26, 32). Here we describe an α_3X variant with a more detailed design of the radical site. Our goal was to develop a system in which the degree of solvent interactions at the phenol OH can be manipulated experimentally. To facilitate subsequent electrochemical analyses of the radical system, it is important to make well-defined structural changes as recently discussed and demonstrated for α_3Y (31, 32) The key challenge is thus to construct a system in which the solvent exposure of the phenol OH is modulated *specifically* while changes in other structural interactions, both global to the protein scaffold and local to the radical site, are *kept to a minimum*. Moving the single tyrosine between different sites in α_3Y is expected to change the solvent exposure of the phenol OH but would most likely also result in significant changes in other interactions, e.g. electrostatic forces, experienced by the phenol ring. For this reason, position 32 was made into a phenol-binding site with the purpose to make the location of the phenol OH group flexible while the location of the aromatic ring itself remains relatively fixed. Figures 1A and B provide a cartoon description of the design behind the mercaptophenol-α_3C (MP-α_3C) proteins (30). It is based on the balance of two predictions: (i) That the hydrophobic packing pattern of the three-helix bundle is maintained (29) and, consequently, that C32 resides inside the folded protein. (ii) That the OH of the ligated phenol is oriented towards the protein surface to minimize the energetic cost of solvating the polar group inside the low-dielectric protein medium. If these predictions hold, the short distance between the OH and the protein-ligating sulfur atom in 2MP will ensure a buried position of the OH (Fig. 1A). In contrast, the longer distance between the OH and SH in 4MP may result in a system where C32 is buried while the phenol OH resides close to or at the protein surface (Fig. 1B). In an earlier report we described a protocol to generate 2-, 3- and 4MP-α_3C and provided a preliminary structural and electrochemical characterization of these three proteins (30). Here we present the solution NMR structure of 2MP-α_3C and confirm the design of the radical site. The structural analysis further suggests a proton-transfer pathway from the buried phenol OH via a hydrogen-bonded glutamate to the bulk solvent. We show that 2MP-α_3C can be reversibly oxidized and reduced and that the phenol has a radical lifetime ($t_{1/2}$) on the ms time scale. We conclude that the 2MP-α_3C system is uniquely suited to electrochemically characterize PCET reactions associated with phenol oxidation and reduction in a well-defined protein environment.

MATERIALS AND METHODS

Expression and purification of α_3C

α_3C was expressed as a thioredoxin fusion using a modified pET15 vector (Novagen) transformed into BL21-CodonPlus(DE3)-RIL (Stratagene). Cells were induced with 1 mM IPTG for 3 hours at 37° C in LB medium or for 24 hours at 30° C in minimal medium containing $^{15}NH_4Cl$ and uniformly labeled ^{13}C glucose (Cambridge Isotope Laboratories). Minimal medium containing $^{15}NH_4Cl$, 10% ^{13}C-labeled glucose and 90% unlabeled glucose provided the samples used for prochiral methyl assignments (33). Harvested cells were resuspended in 20 mM Tris-HCl, 500 mM NaCl, 5 mM imidazole, pH 7.9, treated with lysozyme for 30 minutes and lysed by sonication. The lysate was clarified by centrifugation, passed over a nickel column (His•bind resin, EMD Millipore), and the thioredoxin-α_3C fusion protein eluted by a 0–400 mM imidazole gradient. Thrombin (T6634; Sigma-Aldrich) was added to the fusion protein fraction and the resulting mixture dialyzed against 50 mM Tris-HCl, 500 mM NaCl, 2.5 mM $CaCl_2$, pH 8.0 at room temperature overnight. The digestion mixture was passed over a second nickel column to remove the His-tagged thioredoxin and any remaining undigested fusion protein. α_3C was isolated by reverse-phase HPLC (TP2181010 column; Grace/Vydac) using an acetonitrile/water gradient containing 0.1% (w/v) trifluoroacetic acid and stored as lyophilized powder.

Preparation of 2-mercaptophenol-α_3C

Lyophilized α_3C was dissolved in 50 mM potassium phosphate, 3.0 M guanidinium hydrochloride, pH 8.0. Dithiothreitol was added at an estimated 5-10 fold excess and the mixture incubated for 15 minutes at room temperature. The buffer was exchanged using PD-10 columns (GE Healthcare) equilibrated in 50 mM potassium phosphate, pH 8.0, and the protein concentration determined immediately by Ellman's assay (5,5′ dithiobis (2-nitrobenzoic acid); Sigma-Aldrich; 34) under denaturing conditions and using an ε_{412} of 37000 M^{-1} cm^{-1}. The binding reaction was prepared as follows: 1 part α_3C dissolved in 50 mM potassium phosphate, 10 parts 2-mercaptohenol (Sigma-Aldrich) and 3 M guanidinium hydrochloride. The pH was adjusted to 8.0 and the sample placed on a rotisserie at 4° C overnight. The binding mixture was dialyzed against 50 mM acetate, 30 mM KCl, pH 6.0 at 4° C for 24 hours, purified by reverse-phase HPLC, and the 2MP-α_3C protein stored as lyophilized powder. The concentration of 2MP-α_3C was determined using an ε_{290} of 3700 M^{-1} cm^{-1} (30).

NMR spectroscopy

NMR spectra were collected at 25° C on a 500 MHz Bruker Advance III spectrometer (pulsed field gradient diffusion experiments) and at 30° C on a 750 MHz Varian Inova spectrometer (all other experiments). Both spectrometers were equipped with cold probes. Sample conditions were as follows: (i) Pulsed field gradient diffusion experiments, 440 μM 2MP-α_3C in 20 mM deuterated sodium acetate, 20 mM potassium phosphate, 20 mM sodium borate, 80 mM KCl, 5% D_2O, pH* 6.6 (glass electrode pH reading uncorrected for deuterium isotope effects); (ii) 2D ^1H ^1H NOESY, 800 μM 2MP-α_3C in 30 mM deuterated sodium acetate, 30 mM KCl, 250 μm 4,4-dimethyl-4-silapentane-1-sulfonic acid (DSS), 99.99% D_2O, pH* 5.5; (iii) prochiral methyl assignments, 800 μM 10% ^{13}C-labeled 2MP-α_3C in 30 mM deuterated sodium acetate, 30 mM KCl, 250 μm DSS, 99.99% D_2O, pH* 5.5; (iv) all other experiments, 800 μM ^{13}C,^{15}N labeled 2MP-α_3C dissolved in 30 mM deuterated sodium acetate, 30 mM KCl, 250 μm DSS, pH* 5.5 buffer containing either 10% D_2O or 99.99% D_2O. Pulsed field gradient diffusion experiments to measure the diffusion coefficient of 2MP-α_3C were conducted as described in Ref. 35. Backbone N, H, C, CA and sidechain CB resonance assignments were derived from analyses of triple resonance three-dimensional HNCO, HNCACB and CBCA(CO)NH experiments (36). Sidechain resonance

assignments were obtained from 3D CC(CO)NH-TOCSY, H(CC)(CO)NH-TOCSY and HCCH-TOCSY data (36). The completeness of the backbone (99%) and sidechain (96%) resonance assignments was evaluated using the Assignment Validation Suite (AVS) webserver (37). Prochiral methyl assignments (100% completeness) were performed using the trace glucose labeling strategy (33). Backbone φ and ψ torsion angle restraints were obtained from backbone N, C, CA, HA and sidechain CB chemical shifts using TALOS (38). The predicted φ angles were confirmed by an 3D HNHA experiment (39). NOE distance restraints were derived from 3D NOESY-^{15}N,^{1}H-HSQC (collected in H_2O) and 4D ^{13}C,^{1}H-HMQC-NOESY-^{13}C,^{1}H-HMQC (collected in D_2O) spectra (36, 40). NOEs between protons associated with the 2-mercaptophenol ring and aliphatic protons were obtained from 2D ^{1}H-^{1}H NOESY and 3D NOESY-^{13}C,^{1}H-HSQC data (collected in D_2O; 36). The mixing time was 140 ms for all NOESY experiments. Proton chemical shifts were referenced to DSS directly and ^{13}C and ^{15}N chemical shifts indirectly. NMR data were processed using Felix95 (Accelrys Inc., San Diego, CA) and analyzed with SPARKY (41).

Structure calculations

Structures were generated from experimental NMR restraints by simulated annealing molecular dynamics using the Crystallography & NMR System (CNS) software (42). NOE-derived proton-proton distance restraints were grouped in distance ranges of 1.7–3.0 Å, 1.7–4.0 Å and 1.7–5.0 Å corresponding to strong, medium and weak NOE cross-peak intensities, respectively. When one or two methyl groups were involved, the upper boundary was increased by 0.5 Å and 1.0 Å, respectively. Backbone torsion angle and H-bond restraints were derived from the secondary structure predictions made by the TALOS/HNHA analysis. One thousand trial structures were generated and further evaluated using the CNS accept.inp script to obtain a collection of 141 refined structures. The 32 lowest energy structures from this collection form the deposited structural ensemble. Solvent accessible surface area (SASA) analyses were performed using MOLMOL (43) and a Random Coil Index analysis was performed using the RCI webserver (44). Structural depictions were generated using PyMOL (Schrödinger, LLC).

Data deposition

NMR chemical shifts have been deposited in the BMRB Biological Magnetic Resonance databank (www.bmrb.wisc.edu; accession number 18703). Coordinates of the 32 lowest energy structures have been deposited in the RCSB Protein Data Bank (www.rcsb.org; structure ID 2LXY). In the BMRB and RCSB databanks the covalently attached 2-mercaptophenol is treated as a ligand named HTS with a residue sequence number of 101. Table S1 in the Supporting Information correlates the residue and atom designations used in the BMRB and RCSB databanks with the nomenclature used here and in our earlier study on 2MP-α_3C (30).

Electrochemistry

Differential pulse voltammetry (DPV; 45, 46) and square-wave voltammetry (SWV; 46-48) were performed using an Autolab PGSTAT12 potentiostat equipped with a temperature-controlled, Faraday-cage protected three-electrode micro-cell (Princeton Applied Research). The Ag/AgCl reference electrode and the platinum wire counter electrode (Advanced Measurements Inc.) were stored dry and prepared by filling the former with a 3M KCl/saturated AgCl solution and the latter with sample buffer. All measurements were carried out using a 3 mm diameter pyrolytic graphite edge (PGE) working electrode (Bio-Logic, USA). The electrode surface was activated between measurement by manually polishing its surface for 60 sec. in a 1.0 μm diamond/water slurry on a diamond polishing pad (Bio-Logic, USA) followed by 60 sec. in a 0.05 μm alumina/water slurry on a microcloth pad

(Bioanalytical systems Inc.). The electrode was rinsed with an excess of methanol followed by milli-Q water directed against the surface of the electrode. Measurements were performed immediately following the polishing procedures. The electrochemical cell was also fitted with a pH electrode (Microelectrodes Inc.) connected to a SevenMulti pH meter (Mettler Toledo). The pH electrode was disconnected from the pH meter during the active measurements to avoid the risk of introducing electric noise. The response and reproducibility of the fully assembled electrochemical cell were checked at the beginning of each experimental day by using standard samples and settings. iR compensation was performed by using the Autolab positive feed-back function. Potentials are given *vs.* the normal hydrogen electrode (NHE). All samples were prepared from ultra-pure chemicals and the measurements performed under an argon atmosphere. Salt and protein concentration series were obtained by equal-volume titrations. Data processing and analyses were performed using the Autolab GPES software, KaleidaGraph (Synergy Software) and PeakFit (Systat Software Inc.).

RESULTS

Solution NMR structure of 2MP-α_3C

A key criterion for the α_3X model system is that the constructed macromolecules are valid biomimics for natural proteins. Heteronuclear multidimensional NMR spectroscopy was employed to confirm that this standard holds for 2MP-α_3C. Sample conditions and experiments used for obtaining resonance assignments and experimental restraints are described in the Materials and Methods section. The resonance assignments of 2MP-α_3C were essentially complete (99% of backbone atoms and 96% of sidechain atoms) and have been deposited at the BMRB (accession number 18703). The NOE distance, backbone dihedral angle and H-bond restraints employed for the structure calculations are summarized in Table 1. The CNS software package was used to calculate trial structures by simulated annealing molecular dynamics (42). The calculations were based on an average of 14.8 experimental restraints per residue of which 2.9 represent long-range inter-helical distances. The collection of calculated trial structures was evaluated and refined using the CNS accept.inp script to generate the final 32-membered ensemble that represents the solution structure of 2MP-α_3C. Figure 2 illustrates 2MP-α_3C as a mainchain superposition of the deposited structural ensemble (PDB ID 2LXY) and as a ribbon cartoon displaying the 2-mercaptophenol-C32 (2MP-C32) sidechain. The structure is of excellent quality and displays minimal deviations from experimental restraints and idealized covalent geometries, as shown in Table 1. The RMSD to the mean coordinates is 0.46 Å for backbone atoms and 0.95 Å when included all heavy atoms. MOLMOL (43) identified three α-helices and they are shown in green (residue V2–K17), blue (R24–E41) and purple (V48–K64) in Scheme 1 and in Fig. 2. For the α-helical regions, the RMSD is 0.27 Å for backbone atoms and 0.90 Å for all heavy atoms. The protein is 78% α-helical (51 of 65 residues), which is consistent with earlier CD measurements on 2MP-α_3C (78-81% helix; 30) and the NMR structure of α_3W (51 helical residues of 65 in total; 29). Helices in structured proteins are characterized by a uniformly stable central region flanked by stretches of decreasing stability that give rise to increasing hydrogen exchange rates (49), more extensive averaging of the three-bond HN–HA *J*-coupling constants dependent upon backbone torsion angles (50), and an increasing random coil index (RCI; 44). This pattern is clearly observed for the $^3J_{HNHA}$ coupling constants (39) and RCI values (44) obtained for 2MP-α_3C (Table S2 in the Supporting Information).

The formation of an α-helical bundle is largely driven by the hydrophobic residues that are placed in the heptad *a* and *d* positions (shown in bold in Scheme 1; 28). These residues are predicted to form stacked three-residue packing layers that together constitute a significant

part of the protein hydrophobic core. A solvent accessible surface area (SASA) analysis of the 2MP-α_3C structure is presented in Tables S3 and S4 in the Supporting Information. The heptad *a* and *d* residues form a consistent pattern of low SASA values (Table S3). The protein core contains overall six stacked inter-helical layers: (V2, L42, V48), (L5, I39, V51), (V9, L35, V55), (L12, 2MP-C32, L58), (V16, L28, I62) and (L19, I25, L65). Figure 3 displays the (V16, L28, I62) and (V9, L35, V55) core layers as an illustration. The average RMSD to the mean coordinates is 0.49 Å for the heavy atoms in these 18 residues. Thus, the hydrophobic core of 2MP-α_3C is highly structured and well defined.

Architecture of the phenol radical site

The 2MP-C32 sidechain is found sandwiched between helices 1 and 2 (Fig. 2B). The buried position of the C32 residue (SASA 0 ± 0%) forces the polar OH group of the attached phenol inside the protein, as designed. The average SASA for the atoms associated with 2MP-C32 are summarized in Fig. 4 and listed in more detail in Table S4. The average SASA across the structural ensemble is 3.5 ± 0.7% for the whole residue, 2.0 ± 3.1% for the phenol oxygen, and 4.0 ± 5.4% for the phenol hydroxyl proton. The NMR structure also reveals that the phenol is involved in an inter-helical hydrogen bond to E13 (Fig. 4B). The phenol oxygen/E13 carboxyl oxygen distance is 3.2 ± 0.5 Å across the NMR family of structures. E13 has an average SASA of 12.1 ± 2.6%, which is significantly lower than the other 16 Glu residues in 2MP-α_3C (Table S3). On the atom level, the solvent exposure is located at the carboxyl carbon and oxygen atoms (CD, OE1 and OE2; Fig. 4B and Table S4). Interestingly, this suggests a proton-transfer pathway between the buried phenol OH and the bulk solvent via the E13 carboxyl group. The impact of this interaction on the phenol redox chemistry will be the focus of follow-up voltammetry studies. However, a first step is to show that 2MP-α_3C is an electrochemically reversible system. This is demonstrated below.

SWV analysis of 2MP-α_3C

Square-wave voltammetry (SWV) is a sensitive and diagnostic method for the investigation of various electrochemical processes. Analytical procedures to study adsorption or diffusion-controlled reversible, quasi-reversible and irreversible electrode processes are well documented (46-48). Theoretical methods have been developed to simulate electrode processes that are coupled to preceding or following homogenous chemical reactions (51-54). In SWV, the applied potential is stepped progressively in fixed increments (E_{step}), and at each increment, a forward (in this study, oxidative) potential pulse is applied followed by a reverse (reductive) pulse. The current is sampled at the end of each alternating pulse and traced out as a function of E_{step}. This generates a forward (I_{for}), a reverse (I_{rev}) and a net ($I_{net} = I_{for} - I_{rev}$) voltammogram. The SW frequency ($f = 1/2t_p$) determines the length of the applied pulse (t_p). t_p represents the effective time scale of the experiment and can technically be varied between 62.5 ms (8 Hz) and 250 μs (2000 Hz).

2MP-α_3C was expected to follow an EC mechanism where the observed voltammogram reflects electrode-driven electron transfers, coupled protonic reactions at the phenol oxygen and possible side reactions by the generated radical. The key purpose here was to identify a frequency range where the influence on the voltammogram by the putative radical side reactions is small or removed altogether (i.e., where $t_p \ll t_{1/2}$ associated with the radical side reactions). Voltammograms generated at such conditions will be dominated by the thermodynamic and kinetic properties of the electrode process (i.e. phenol PCET) and not by homogenous side reactions. The SWV analysis involved optimization and characterization of the 2MP-α_3C Faradaic current followed by collecting SW frequency data series.

2MP-α_3C/PGE electrode optimization and evaluation

The electrochemical analysis of 2MP-α_3C required a pyrolytic graphite "edge" (PGE) working electrode in order to generate SWV data with good signal-to-noise (S/N). A set of experiments was conducted to optimize and characterize the Faradaic response from 2MP-α_3C on a PGE electrode. These studies are described in detail in the Supporting Information and provided the following key results: (i) 20 mM APB (acetate, phosphate, borate) buffer, 40 – 140 mM KCl, 20 – 100 μM protein yield voltammograms with optimal S/N at both acidic and alkaline pH (Fig. S1). At these conditions, (ii) E_{peak} is not influenced by the chemical groups present at the electrode surface (Figs. S1A and B), (iii) diffusion-controlled electrode kinetics is observed (Fig. S1C), (iv) 2MP-α_3C does not unfold on the electrode surface and (v) the oxidized protein is not involved in intermolecular radical-radical or radical-substrate reactions (Fig. S1B). Square-wave voltammograms were collected on 2MP-α_3C, α_3C (i.e. the protein scaffold without the ligated phenol), and plain buffer at the conditions optimized for the PGE electrode (Fig. S2). Consistent with the assignment of the voltammogram to the protein-bound phenol (30), a Faradaic current is uniquely observed for 2MP-α_3C while the α_3C voltammograms closely resemble the baseline buffer traces. A high level of reproducibility was observed for data replicates and independently obtained 2MP-α_3C voltammograms (Fig. S4). The average errors in E_{peak} (≤ ± 5 mV) and half-height peak widths (≤ ± 5 mV) were small. The peak amplitude and the S/N are both sensitive to the SW frequency with a small Faradaic current at low frequencies (≤ 60 Hz) and an increase in noise at high frequencies (≥ 540 Hz). The average error in I_{net} was about ± 10%.

2MP-α_3C gives rise to reversible phenol voltammograms

Figure 5 shows background-corrected forward and reverse SW voltammograms collected at 190, 540 and 720 Hz at pH 8.51 (top row) and pH 5.52 (bottom row). The forward and reverse voltammograms represent the oxidative and reductive currents, respectively. The two pH data sets display the same trend of changing from quasi-reversible to reversible as the frequency increases. E_{net} is highly insensitive to the frequency and increases by only 3 ± 2 mV (pH 8.51) and 6 ± 2 mV (pH 5.52) as the frequency is changed from 190 to 720 Hz. The I_{for}/I_{rev} ratio decreases from 1.2 (pH 8.51) and 1.3 (pH 5.52) to a limiting value of 1.0 at ≥ 540 Hz. $\Delta E = E_{for} - E_{rev}$ decreases from – 17 ± 2 mV to – 4 ± 2 mV (pH 8.51) and from – 12 ± 2 mV to 2 ± 2 mV (pH 5.52). Figure 6 illustrates the changes in the properties of the high-pH 2MP-α_3C voltammogram in more detail and over a broader frequency range (30 to 720 Hz). Figure 6A shows that E_{net} is 847 ± 2 mV (over a 120 – 720 Hz range), E_{for} is 844 ± 2 mV (440 – 720 Hz), and E_{rev} is 851 ± 2 mV (440 – 720 Hz) at pH 8.51 ± 0.01. This is consistent with a fully reversible diffusion-controlled electrode process, which is characterized by peak potentials that are independent of the SW frequency and separated by only a few mV (47-48). Figure 6B shows that I_{net} increases as a function of the frequency and reaches a maximum in the 440 – 720 Hz range. This observation is consistent with SWV simulations of EC systems where the coupled chemical reactions are so slow relative to the time scale of the experiment that they have no impact on the voltammogram (51-54). We also observe that the I_{for}/I_{rev} ratio declines as the frequency increases and reaches a limiting value of 1.0 at ≥ 440 Hz (Fig. 6C). We conclude that the 2MP-α_3C electrode process is reversible at SW frequencies above ~ 500 Hz at both pH 8.5 and 5.5.

DISCUSSION

Tyrosine oxidation-reduction occurs as a PCET process where the e^-/H^+ loss or gain may take place as a single event (concerted electron proton transfer, CEPT) or follow a stepwise pathway (electron proton transfer or proton electron transfer). CEPT avoids high-energy intermediates but requires a spatially well-organized site. The larger mass of the proton relative to the electron makes the proton-tunneling component of the CEPT process highly

dependent on structural details. The electron and proton acceptor/donor can be separate molecules or a single molecular center. Examples of the former situation include oxidation of Y_Z and Y_D in photosystem II (the photo-oxidized chlorophyll complex $P680^+$ serves as the oxidant; a H-bonded His serves as the primary proton acceptor; 1, 55-57) and oxidation-reduction of Y356-β in ribonucleotide reductase (multistep ET via Y356-β; proton acceptor/donor possibly E350-β; 58, 59). An example of the latter situation includes e.g. reduction of the catalytically active Y385 radical in prostaglandine H synthase (net e^-/H^+ transfer from the fatty acid substrate to Y385–O$^\bullet$; 60). The general consensus emerging from studies on enzymes and model systems is that tyrosine oxidation, and most likely also the reduction, occurs as a CEPT process in the majority of systems (18). The MP-α_3C proteins were constructed to electrochemically characterize phenol oxidation and reduction in a structured protein environment with specific emphasis on the protonic reactions occurring at the phenol oxygen (30). This study describes several significant steps towards this goal, as discussed below.

2MP-α_3C displays key biomimetic properties

2MP-α_3C is a stable, uniquely structured three-helix bundle with a well-defined hydrophobic core. The model protein displays structural characteristics that are fully consistent with properties observed for native proteins. We note that the structural ensemble of an aqueous “peptide” would typically reflect a population distributed across a more shallow energy landscape relative to the energy landscape of a uniquely structured protein. Consequently, a radical generated in a peptide scaffold resides in an environment in which structural interactions and solvent exposure are less well defined and less well controlled. The classic “protein” properties observed for 2MP-α_3C are likely to play a significant role in the stabilization of the radical state (*vide infra*).

2MP-α_3C was designed to specifically shield the phenol OH group from the bulk solvent (Fig. 1A; 30). The solution NMR structure of 2MP-α_3C verifies the design of the radical site (Fig. 4A). Only 3.5 ± 0.7% of 2MP-C32 is solvent exposed and the phenol OH group has an average SASA of 3.0 ± 4.5% (Table S4). The NMR structure also reveals that the phenol forms an inter-helical hydrogen bond to E13 (Fig. 4B). It is likely that E13 is involved in rapid de- and/or reprotonation reactions associated with the electrode-driven oxidation-reduction of 2MP-C32. As discussed below, the pH dependence of the 2MP-C32 potential is consistent with an overall charge neutral system, i.e., the phenol site is in equilibrium with the bulk phase on the time scale of the experiment. The SASA analysis shows that the solvent exposure of the phenol OH and the carboxyl oxygens of E13 (37 ± 18%) differ by one order of magnitude. This suggests a redox-driven proton-transfer pathway between the phenol and the bulk solvent. These structural features are most likely tightly connected to the electrochemical reversibility of the phenol oxidation-reduction process. Investigation of these issues is in progress.

Reversible phenol voltammograms provide formal reduction potentials

For a reversible and diffusion-controlled redox system, the peak potential of the SWV net current (E_{net}) equals the formal reduction potential ($E^{0,}$) when the reduced and oxidized species diffuse at equal rates (46). The diffusion coefficient of reduced 2MP-α_3C was determined to $1.4 \pm 0.2 \times 10^{-6}$ cm^2 s^{-1} by pulsed field gradient NMR (Fig. S4; 35). α_3Y exhibits the same rate of diffusion (31), which is typical of a small globular protein. The diffusion coefficient of 2MP-α_3C is not expected to change significantly as a function of redox state (loss/gain of one e^-/H^+). We conclude that E_{net} (≥ 500 Hz) represents the formal reduction potential of the protein-bound phenol.

The initial characterization of 2MP-α_3C included a differential pulse voltammetry (DPV) study using a glassy carbon (GC) working electrode (30). The DPV/GC study provided three key results: The α_3C scaffold is redox inert (no Faradic current observed), the protein-bound phenol is redox active (Faradaic current observed upon phenol ligation) and the 2MP-α_3C voltammogram represents the neutral phenol-O$^{\bullet}$/phenol OH redox pair (ΔE_{peak} 55 ± 5 mV/pH unit). DPV and SWV are both sensitive methods (minimization of capacitative background currents, peak-shaped response) but only the latter provides a diagnostic tool similar to that of cyclic voltammetry (46). Thus, the preliminary DPV/GC study of 2MP-α_3C (30) did not delineate the electrode process nor exclude the possibility of distorting protein/electrode interactions. Here a pyrolytic graphite edge (PGE) working electrode system was optimized for 2MP-α_3C, which allowed a SWV analysis to be performed. The SWV study reproduced the three DPV results listed above (Figs. S2 and 5; ΔE_{net} 54 ± 5 mV/pH unit). In addition we could show: (i) that E_{net} is not influenced by chemical groups on the working electrode surface, (ii) that the protein does not unfold on the electrode surface, (iii) that the electrode process is reversible and (iv) diffusion controlled, and (v) that E_{net} (≥ 500 Hz) = $E^{0,}$. Comparing the 2MP-α_3C $E_{1/2}$ potential measured with DPV, using either a GC (30) or a PGE (Fig. S1A) electrode, with $E^{0,}$ as determined by SWV reveals that there is no significant difference (9 ± 12 mV). The potential is not influenced by the electrode surface and both DPV and SWV provide the thermodynamically corrected formal potential of the 2MP-α_3C redox system.

2MP-α_3C was made as an analogue for tyrosine radical proteins and $E^{0,}$ values observed for this system are close to those observed for α_3Y (31). $E^{0,}$(pH 8.51 ± 0.02) is 847 ± 2 mV *vs.* NHE for the phenol O$^{\bullet}$/phenol-OH redox couple. This value is about 60 mV lower relative to the $E^{0,}$ of 909 ± 3 mV for the Y32–O$^{\bullet}$/Y32–OH redox pair at the same pH. Thus, both the structural and redox properties of 2MP-α_3C make this protein highly suitable as a biomimetic system for natural tyrosine redox cofactors.

2MP-α_3C contains a long-lived phenol radical

The redox reversibility observed for 2MP-α_3C is rare for a phenol-based system. Solvated tyrosine or phenol gives rise to irreversible voltammograms dominated by rapid intermolecular radical-radical and radical-substrate reactions (61-63). Some sterically protected and H-bonded phenols dissolved in organic solvents give rise to voltammograms that are quasi reversible to various degrees (e.g. 19-25). Such voltammograms reflect electrode-driven oxidation-reduction, coupled protonic reactions at the phenol oxygen and/or radical side reactions. The 2MP-α_3C voltammogram becomes fully reversible ~ 500 Hz and, at these conditions, neither protonic reactions not radical side reactions influence the observed voltammogram. Voltammograms collected < 500 Hz are quasi-reversible and this may arise from the coupled protonic reactions and/or radical side reactions. These observations are consistent with a very long-lived radical state, even if the quasi-reversibility arises mainly from radical side reactions. SWV simulations predict that the influence of coupled chemical reactions on E_{net} approaches zero when $\log(2t_p k_{EC}) \leq -1.5$ (47, 51, 52). There is no significant change in E_{net} > 120 Hz at high pH. This predicts that the rate constant (k_{EC}) associated with side reaction(s) is ≤ 4 s_{-1}, which translates into a radical $t_{1/2}$ of ≥ 180 ms. This is a remarkably long lifetime for an oxidized phenol and still represents only a lower-limit estimate. A similar observation was made for Y32–O$^{\bullet}$, which has a $t_{1/2}$ of ≥ 30 ms (31). To provide a comparison, aqueous tyrosine has a radical $t_{1/2}$ of ~ 10-20 μs at the conditions used here (62). These results highlight the difference between solution redox chemistry and protein redox chemistry.

Concluding remarks

2MP-α_3C was created to gain insights to tyrosine radical cofactors. 2MP-α_3C mimics the biochemical systems in several important ways. It displays structural properties associated with natural proteins. The radical site is shielded and the phenol H-bonded to a Glu. It is generally accepted that the properties of tyrosine redox cofactors critically depend on interactions to a H-bonded proton acceptor/donor. The phenol oxidation-reduction cycle is reversible and occurs in a well-structured environment. The protein matrix stabilizes the radical into the high ms time scale or longer. Most, if not all, PCET-oriented mechanistic studies of tyrosine/phenol model systems have focused on the oxidation side of the redox cycle (18). Loss of the radical state in various side reactions naturally makes it more difficult to investigate the reduction process. 2MP-α_3C provides the unique opportunity to study the electron and proton transfers associated with the reduction process.

Supplementary Material

Refer to Web version on PubMed Central for supplementary material.

Abbreviations

α_3Y, α_3W and α_3C	*de novo* protein containing a single buried tyrosine, tryptophan or cysteine
APB buffer	sodium acetate, potassium phosphate, sodium borate buffer
DPV	differential pulse voltammetry
DSS	4,4 dimethyl-4-silapentane-1-sulfonic acid
$E^{0,}$	formal potential
$E_{1/2}$	voltammetry half-wave potential
EC	electrode process coupled to homogenous chemical reaction
E_{peak}	peak potential
E_{for}, E_{rev} and E_{net}	peak potential of the forward, reverse and net current in SWV
f	square-wave frequency
GC	glassy carbon
pK_{app}	apparent pK_a value
I_{for}, I_{rev} and I_{net}	forward, reverse and net current in SWV
MP	mercaptophenol
PSII	photosystem II
PCET	proton-coupled electron transfer
PGE	pyrolytic graphite edge
SWV	square-wave voltammetry
t_p	pulse width
Y32	redox-active tyrosine in α_3Y
Y_Z and Y_D	redox-active tyrosines in photosystem II

REFERENCES

1. Tommos C, Babcock GT. Proton and hydrogen currents in photosynthetic water oxidation. Biochim. Biophys. Acta. 2000; 1458:199–219. [PubMed: 10812034]
2. Pesavento RP, van der Donk WA. Tyrosyl radical cofactors. Adv. Protein Chem. 2001; 58:317–385. [PubMed: 11665491]
3. Hoganson CW, Tommos C. The function and characteristics of tyrosyl radical cofactors. Biochim. Biophys. Acta. 2004; 1655:116–122. [PubMed: 15100023]
4. Reece SY, Nocera DG. Proton-coupled electron transfer in biology: Results from synergistic studies in natural and model systems. Annu. Rev. Biochem. 2009; 78:673–699. [PubMed: 19344235]
5. Dempsey JL, Winkler JR, Gray HB. Proton-coupled electron flow in protein redox machines. Chem. Rev. 2010; 110:7024–7039. [PubMed: 21082865]
6. Cukier RI, Nocera DG. Proton coupled electron transfer. Ann. Rev. Phys. Chem. 1998; 49:337–369. [PubMed: 9933908]
7. Mayer JM. Proton-coupled electron transfer: A reaction chemist's view. Annu. Rev. Phys. Chem. 2004; 55:363–90. [PubMed: 15117257]
8. Huynh MHV, Meyer TJ. Proton-Coupled Electron Transfer. Chem. Rev. 2007; 107:5004–5064. [PubMed: 17999556]
9. Hammes-Schiffer S, Stuchebrukhov AA. Theory of coupled electron and proton transfer reactions. Chem. Rev. 2010; 110:6939–6960. [PubMed: 21049940]
10. Savéant JM. Electrochemical approach to proton coupled electron transfers: recent advances. Energy Environ. Sci. 2012; 5:7718–7731.
11. Sjödin M, Styring S, Åkemark B, Sun L, Hammarström L. Proton-coupled electron transfer from tyrosine in a tyrosine-ruthenium-tris-bipyridine complex: Comparison with tyrosine$_Z$ oxidation in photosystem II. J. Am. Chem. Soc. 2000; 122:3932–3936.
12. Stubbe J, Nocera DG, Yee CS, Chang MCY. Radical initiation in the class I ribonucleotide reductase: Long-range proton-coupled electron transfer? Chem. Rev. 2003; 103:2167–2202. [PubMed: 12797828]
13. Reece SY, Nocera DG. Direct tyrosine oxidation using the MLCT excited states of rhenium polypyridyl complexes. J. Am. Chem. Soc. 2005; 127:9448–9458. [PubMed: 15984872]
14. Fecenko CJ, Meyer TJ, Thorp HH. Electrocatalytic oxidation of tyrosine by parallel rate limiting proton transfer and multisite electron-proton transfer. J. Am. Chem. Soc. 2006; 128:11020–11021. [PubMed: 16925408]
15. Sibert R, Josowicz M, Porcelli F, Veglia G, Range K, Barry BA. Proton-coupled electron transfer in a biomimetic peptide as a model of enzyme regulatory mechanisms. J. Am. Chem. Soc. 2007; 129:4393–4400. [PubMed: 17362010]
16. Costentin C, Louault C, Robert M, Savéant J-M. The electrochemical approach to concerted proton-electron transfers in the oxidation of phenols in water. Proc. Nat. Acad. Sci. U.S.A. 2009; 106:18143–18148.
17. Pizano AA, Lutterman DA, Holder PG, Teets TS, Stubbe J, Nocera DG. Photo-ribonucleotide reductase beta 2 by selective cysteine labeling with a radical phototrigger. Proc. Nat. Acad. Sci. U.S.A. 2012; 109:39–43.
18. Warren JJ, Winkler JR, Gray HB. Redox properties of tyrosine and related molecules. FEBS Lett. 2012; 586:596–602. [PubMed: 22210190]
19. Maki T, Araki Y, Ishida Y, Onomura O, Matsumura Y. Construction of persistent phenoxyl radical with intramolecular hydrogen bonding. J. Am. Chem. Soc. 2001; 123:3371–3372. [PubMed: 11457075]
20. Benisvy L, Blake AJ, Collison D, Davies ES, Garner CD, McInnes EJL, McMaster J, Whittaker G, Wilson C. A phenol–imidazole pro-ligand that can exist as a phenoxyl radical, alone and when complexed to copper(II) and zinc(II). Dalton Trans. 2003; 10:1975–1985.
21. Rhile IJ, Mayer JM. One-electron oxidation of a hydrogen-bonded phenol occurs by concerted proton-coupled electron transfer. J. Am. Chem. Soc. 2004; 126:12718–12719. [PubMed: 15469234]

22. Costentin C, Robert M, Savéant JM. Electrochemical and homogeneous proton-coupled electron transfers: Concerted pathways in the one-electron oxidation of a phenol coupled with an intramolecular amine-driven proton transfer. J. Am. Chem. Soc. 2006; 128:4552–4553. [PubMed: 16594674]
23. Rhile IJ, Markle TF, Nagao H, DiPasquale AG, Lam OP, Lockwood MA, Rotter K, Mayer JM. Concerted proton-electron transfer in the oxidation of hydrogen-bonded phenols. J. Am. Chem. Soc. 2006; 128:6075–6088. [PubMed: 16669677]
24. Moore GF, Hambourger H, Gervaldo M, Poluektov OG, Rajh T, Gust D, Moore TA, Moore AL. A Bioinspired Construct That Mimics the Proton Coupled Electron Transfer between $P680^{\bullet+}$ and the Tyr_Z-His190 Pair of Photosystem II. J. Am. Chem. Soc. 2008; 130:10466–10467. [PubMed: 18642819]
25. Zhang M-T, Irebo T, Johansson O, Hammarström L. Proton-coupled electron transfer from tyrosine: A strong rate dependence on intermolecular proton transfer distance. J. Am. Chem. Soc. 2011; 133:13224–13227. [PubMed: 21812404]
26. Tommos C, Skalicky JJ, Pilloud DL, Wand AJ, Dutton PL. De novo proteins as models of radical enzymes. Biochemistry. 1999; 38:9495–9507. [PubMed: 10413527]
27. Westerlund K, Berry BW, Privett HK, Tommos C. Exploring amino-acid radical chemistry: protein engineering and de novo design. Biochim. Biophys. Acta. 2005; 1707:103–116. [PubMed: 15721609]
28. DeGrado WF, Summa CM, Pavone V, Nastri F, Lombardi A. De novo design and structural characterization of proteins and metalloproteins. Annu. Rev. Biochem. 1999; 68:779–819. [PubMed: 10872466]
29. Dai Q-H, Tommos C, Fuentes EJ, Blomberg MRA, Dutton PL, Wand AJ. Structure of a de novo designed model protein of radical enzymes. J. Am. Chem. Soc. 2002; 124:10952–10953. [PubMed: 12224922]
30. Hay S, Westerlund K, Tommos C. Moving a phenol hydroxyl group from the surface to the interior of a protein: Effects on the phenol potential and pK_A. Biochemistry. 2005; 44:11891–11902. [PubMed: 16128591]
31. Berry BW, Martínez-Rivera MC, Tommos C. Reversible voltammograms and a Pourbaix diagram for a protein tyrosine radical. Proc. Nat. Acad. Sci. U.S.A. 2012; 109:9739–9743.
32. Martínez-Rivera MC, Berry BW, Valentine KG, Westerlund K, Hay S, Tommos C. Electrochemical and structural properties of a protein system designed to generate tyrosine Pourbaix diagrams. J. Am. Chem. Soc. 2011; 133:17786–17795. [PubMed: 22011192]
33. Neri D, Szyperski T, Otting G, Senn H, Wüthrich K. Stereospecific nuclear magnetic resonance assignments of the methyl groups of valine and leucine in the DNA-binding domain of the 434 repressor by biosynthetically directed fractional ^{13}C labeling. Biochemistry. 1989; 28:7510–7516. [PubMed: 2692701]
34. Ellman GL. Tissue sulfhydryl groups. Arch. Biochem. Biophys. 1959; 82:70–77. [PubMed: 13650640]
35. Zheng G, Price WS. Simultaneous convection compensation and solvent suppression in biomolecular NMR diffusion experiments. J. Biomol. NMR. 2009; 45:295–299. [PubMed: 19697137]
36. Sattler M, Schleucher J, Griesinger C. Heteronuclear multidimensional NMR experiments for the structure determination of proteins in solution employing pulsed field gradients. Prog. Nucl. Magn. Reson. Spectrosc. 1999; 34:93–158.
37. Moseley HNB, Sahota G, Montelione GT. Assignment validation software suite for the evaluation and presentation of protein resonance assignment data. J. Biomol. NMR. 2004; 28:341–355. [PubMed: 14872126]
38. Cornilescu G, Delaglio F, Bax A. Protein backbone angle restraints from searching a database for chemical shift and sequence homology. J. Biomol. NMR. 1999; 13:289–302. [PubMed: 10212987]
39. Vuister GW, Bax A. Quantitative *J* correlation: A new approach for measuring homonuclear three-Bond $J(H^NH^\alpha)$ coupling constants in ^{15}N-enriched proteins. J. Am. Chem. Soc. 1993; 115:7772–7777.

40. Clore GM, Kay LE, Bax A, Gronenborn AM. Four-dimensional $^{13}C/^{13}C$-edited Nuclear Overhauser Enhancement Spectroscopy of a protein in solution: Application of interleukin 1•. Biochemistry. 1991; 30:12–18. [PubMed: 1988012]
41. Goddard, TD.; Kneller, DG. SPARKY 3. University of California; San Francisco: 2008.
42. Brunger AT, Adams PD, Clore GM, DeLano WL, Gros P, Grosse-Kunstleve RW, Jiang JS, Kuszewski J, Nilges M, Pannu NS, Read RJ, Rice LM, Simonson T, Warren GL. Crystallography & NMR system: A new software suite for macromolecular structure determination. Acta Crystallogr. D-Biol. Cryst. 1998; 54:905–921. [PubMed: 9757107]
43. Koradi R, Billeter M, Wüthrich K. MOLMOL: A program for display and analysis of macromolecular structures. J. Mol. Graph. 1996; 14:51–52. [PubMed: 8744573]
44. Berjanskii MV, Wishart DS. A simple method to predict protein flexibility using secondary chemical shifts. J. Am. Chem. Soc. 2005; 127:14970–14971. [PubMed: 16248604]
45. Parry EP, Osteryoung RA. Evaluation of analytical pulse polarography. Anal. Chem. 1965; 37:1634–1637.
46. Bard, AJ.; Faulkner, LR. Electrochemical methods: Fundamentals and applications. 2nd Ed. John Wiley & Sons, Inc.; USA: 2001.
47. Osteryoung, J.; O'Dea, JJ. Square-wave voltammetry, in *Electroanalytical chemistry*. Bard, AJ., editor. Vol. 5. Marcel Dekker; New York: 1986. p. 209-308.
48. Mirčeski, V.; Komorsky-Lovrić, Š.; Lovrić, M. Square-wave voltammetry: Theory and applications. In: Scholz, F., editor. Monographs in electrochemistry. Springer Verlag; Berlin, Germany: 2007.
49. Wand AJ, Roder H, Englander SW. Two-dimensional H^1-NMR studies of cytochrome-c – Hydrogen-exchange in the N-terminal helix. Biochemistry. 1986; 25:1107–1114. [PubMed: 3008820]
50. Pardi A, Billeter M, Wüthrich K. Calibration of the angular dependence of the amide proton-C^a proton coupling constants, $^3J_{HN\alpha}$, in a globular protein. J. Mol. Biol. 1984; 180:741–751. [PubMed: 6084720]
51. O'Dea JJ, Osteryoung J, Osteryoung RA. Theory of square wave voltammetry for kinetic systems. Anal. Chem. 1981; 53:695–701.
52. Miles AB, Compton RG. Simulation of square-wave voltammetry: EC and ECE electrode processes. J. Phys. Chem. B. 2000; 104:5331–5342.
53. Garay F, Milivoj Lovrić M. Square-wave voltammetry of quasi-reversible electrode processes with coupled homogeneous chemical reactions. J. Electroanal. Chem. 2002; 518:91–102.
54. Rudolph M. Digital simulation with the fast implicit finite difference (FIFD) algorithm. Part 5: Digital simulations of square wave voltammetry for any user defined electrochemical mechanism comprising first- and second-order chemical reactions. J. Electroanal. Chem. 2001; 503:15–27.
55. Hays A-MA, Vassiliev IR, Golbeck JH, Debus RJ. Role of D1-His190 in the proton-coupled oxidation of tyrosine Y_Z in manganese-depleted photosystem II. Biochemistry. 1999; 38:11851–11865. [PubMed: 10508388]
56. Umena Y, Kawakami K, Shen JR, Kamiya N. Crystal structure of oxygen-evolving photosystem II at a resolution of 1.9Å. Nature. 2011; 473:55–60. [PubMed: 21499260]
57. Keough JM, Jenson DL, Zuniga AN, Bary BA. Proton coupled electron transfer and redox-active tyrosine Z in the photosynthetic oxygen-evolving complex. J. Am. Chem. Soc. 2011; 133:11084–11087. [PubMed: 21714528]
58. Reece SY, Hodgkiss JM, Stubbe J, Nocera DG. Proton-coupled electron transfer: The mechanistic underpinning for radical transport and catalysis in biology. Phil. Trans. R. Soc. B. 2006; 1472:1351–1364. [PubMed: 16873123]
59. Yokoyama K, Smith AA, Corzilius B, Griffin RG, Stubbe J. Equilibration of tyrosyl radicals ($Y_{356}^{\bullet}$, $Y_{731}^{\bullet}$, $Y_{730}^{\bullet}$) in the radical propagation pathway of the *escherichia coil* class la ribonucleotide reductase. J. Am. Chem. Soc. 2011; 133:18420–18432. [PubMed: 21967342]
60. Tsai A-L, Kulmacz RJ. Prostaglandin H synthase: resolved and unresolved mechanistic issues. Arch. Biochem. Biophys. 2010; 493:103–124. [PubMed: 19728984]
61. Mahoney LR, DaRooge MA. Kinetic behavior and thermochemical properties of phenoxy radical. J. Am. Chem. Soc. 1975; 97:4722–4731.

62. Hunter EPL, Desrosiers MF, Simic MG. The effect of oxygen, antioxidants, and superoxide radical on tyrosine phenoxyl radical dimerization. Free Rad. Biol. Med. 1998; 6:581–585. [PubMed: 2546863]

63. Ye M, Schuler RH. Second-order combination reactions of phenoxyl radicals. J. Phys. Chem. 1989; 93:1898–1902.

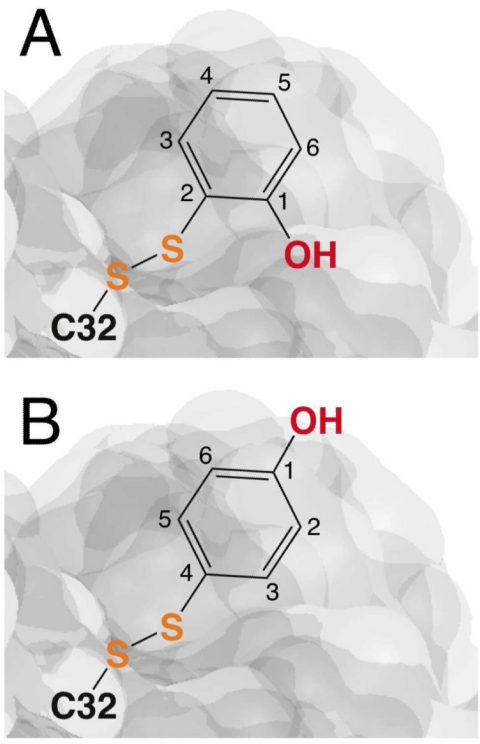

Figure 1.
Cartoon description of the (A) 2-mercaptophenol-α_3C (2MP-α_3C) and (B) 4-mercaptophenol-α_3C (4MP-α_3C) protein design (30). The main purpose when constructing these proteins was to make significant changes in the solvent exposure of the phenol OH group while keeping other structural changes, both in the overall protein scaffold and at the radical site, to a minimum.

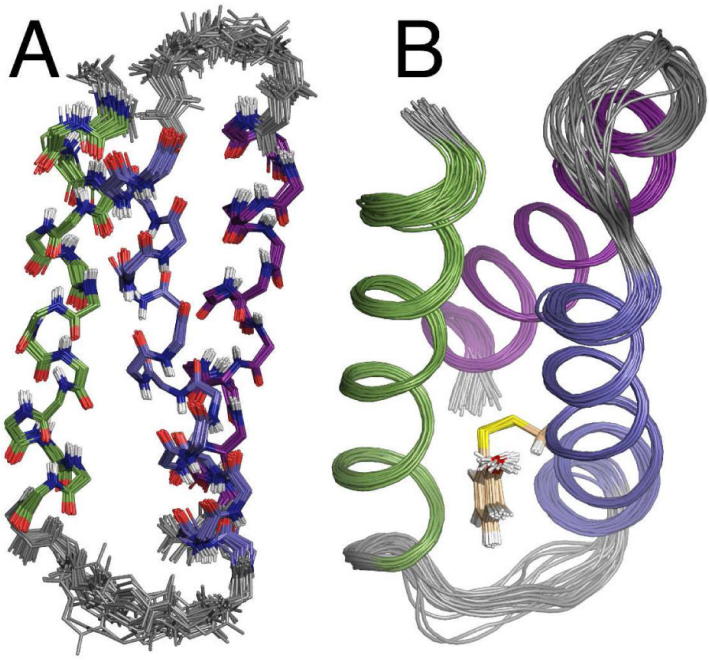

Figure 2.

Solution NMR structure of 2MP-α_3C displayed (A) as a backbone (N, H, C, O, CA) superposition of the final ensemble of 32 simulated annealing structures and (B) as a ribbon cartoon with the sidechain of the modified 2-mercaptophenol-C32 (2MP-C32) residue. Helix 1 (residue V2–K17) is colored green, helix 2 (R24–E41) blue, and helix 3 (V48–K64) purple. Non-helical loop regions are shown in grey. See Table 1 for a summary of the NMR experimental restraints and structural statistics.

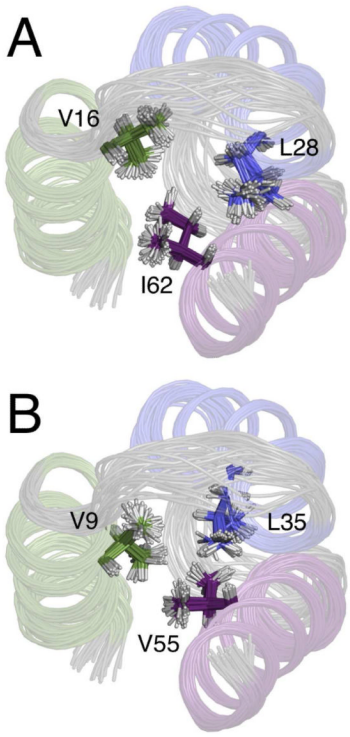

Figure 3.
Residues (A) V16, L28 and I62 and (B) V9, L35 and V55 participate in two of the six inter-helical packing layers that form a major part of the 2MP-α_3C hydrophobic core.

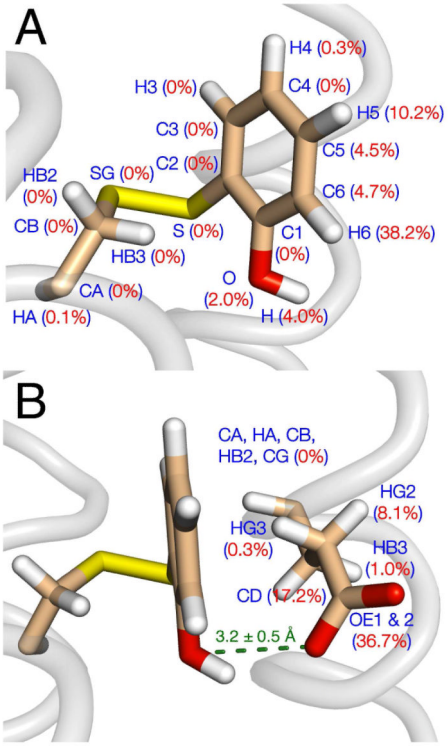

Figure 4.

Average solvent accessible surface areas for atoms associated with the hydrogen-bonded 2MP-C32 and E13 pair (see Table S4 for additional SASA information). The average O/O distance between the phenol oxygen and the closest E13 carboxyl oxygen is 3.2 ± 0.5 Å. The nomenclature used for (A) 2MP-C32 is based on labeling the modified cysteine/phenol residue as an unnatural tyrosine analogue with backbone atoms derived from C32 and sidechain atoms derived from both C32 and the S–S ligated phenol. For the deposited data, convention requires that the covalently attached phenol is labeled as a ligand (name HTS, sequence residue number 101). Table S1 provides a guide correlating the residue and atom designations used in the BMRB and the Protein Data Bank with the nomenclature used here and in Ref. 30. (B) The E13 SASA pattern suggests a proton-transfer pathway between the buried phenol OH via the E13 carboxyl group to the bulk solution.

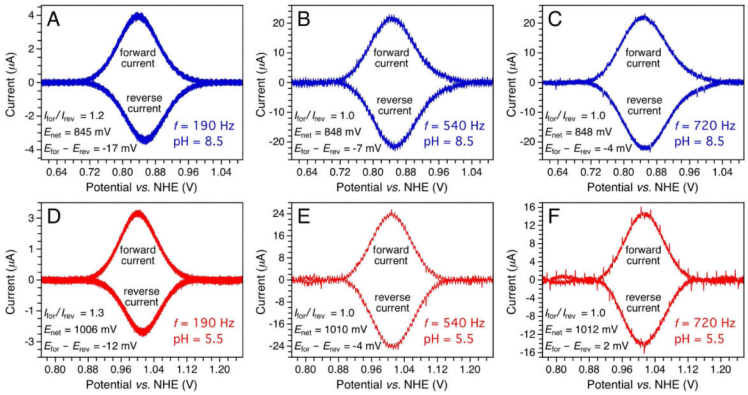

Figure 5.

Background-corrected forward and reverse square-wave voltammograms obtained from 2MP-α_3C using a SW frequency of (panels A and D) 190 Hz (t_p 2.6 ms), (B and E) 540 Hz (t_p 926 μs), and (C and E) 720 Hz (t_p 694 μs). The voltammograms displayed in panels A to C were obtained at pH 8.51 ± 0.02 and those displayed in D to F at pH 5.52 ± 0.01. SWV settings: 75 μM 2MP-α_3C in 20 mM APB, 80 mM KCl; PGE working electrode, temperature 25° C, step potential 0.15 mV, SW pulse amplitude 25 mV.

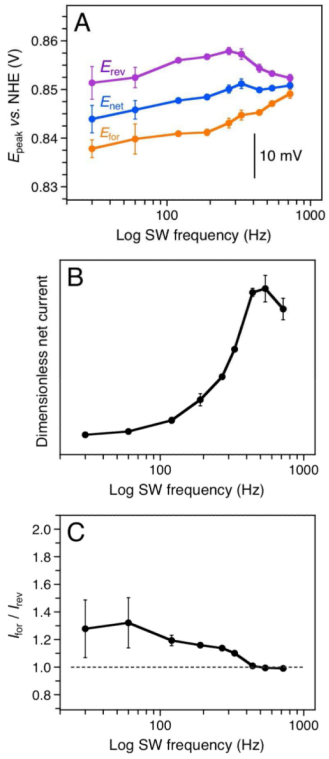

Figure 6.

Changes in the (A) peak potential of the net (E_{net}), forward (E_{for}) and reverse (E_{rev}) 2MP-α_3C voltammogram as a function the SW frequency. (B) Dimensionless I_{net} and (C) I_{for}/I_{rev} ratio as a function of the SW frequency. The dimensionless net current was calculated as described in Ref. 46 and using a diffusion coefficient of $1.4 \pm 0.2 \times 10^{-6}$ cm^2 s^{-1} (Fig. S5). SWV settings: 75 μM 2MP-α_3C in 20 mM APB, 80 mM KCl, pH 8.51 ± 0.02; PGE working electrode, temperature 25° C, step potential 0.15 mV, SW pulse amplitude 25 mV.

Table 1

Experimental restraints and structural statistics for the solution NMR 2MP-α_3C structure

Experimental restraints	
NOE – intra-residue	216
NOE – sequential (| *i–j* | = 1)	222
NOE – medium range (1 < | *i–j* | < 5)	181
NOE – long range (| *i–j* | ≥ 5)	190
NOE restraints – All	809
Backbone dihedral angles	107
Hydrogen bonds	44
Experimental restraints – All	960
Restraints per residue	14.8
Long-range restraints per residue	2.9
Residual restraints violations	
NOE distance > 0.1 Å	0
Backbone dihedral angle > 2°	0
Number of structures in ensemble	32
RMSD from experimental restraints	
NOE distance deviation (Å)	0.0061 ± 0.0003
Maximum NOE distance deviation (Å)	0.079
Backbone angle deviation (°)	0.221 ± 0.019
Maximum backbone angle deviation (°)	1.2
RMSD from idealized covalent geometry	
Bonds (Å)	0.0011 ± 0.0001
Angles (°)	0.331 ± 0.004
Impropers (°)	0.202 ± 0.009
Ramachandra plot statistics	
Most favoured regions (%)	96.4
Additionally allowed regions (%)	3.2
Generously allowed regions (%)	0.3
Disallowed regions (%)	0
RMSD to average coordinates	
Backbone atoms (Å) (residue 1-65)	0.464
All heavy atoms (Å) (residue 1-65)	0.949
Backbone atoms (Å) (residue 2-17, 24-41,	0.273
All heavy atoms (Å) (residue 2-17, 24-41,	0.901